Appendix 2 ITRF2014 JGR paper

AGU PUBLICATIONS

JGR

Journal of Geophysical Research: Solid Earth

RESEARCH ARTICLE
10.1002/2016JB013098

ITRF2014: A new release of the International Terrestrial Reference Frame modeling nonlinear station motions

Zuheir Altamimi[1], Paul Rebischung[1], Laurent Métivier[1], and Xavier Collilieux[2]

[1]IGN LAREG, Université Paris Diderot, Paris, France, [2]Institut National de l'Information Géographique et Forestière, Service de la géodésie et du nivellement, Saint-Mandé, France

Key Points:
- ITRF2014 benefits from accurate modeling of station annual and semiannual displacements
- ITRF2014 benefits from accurate modeling of postseismic deformations for sites affected by major earthquakes
- Leading to the determination of accurate and robust secular frame and site velocities

Correspondence to:
Z. Altamimi,
zuheir.altamimi@ign.fr

Citation:
Altamimi, Z., P. Rebischung, L. Métivier, and C. Xavier (2016), ITRF2014: A new release of the International Terrestrial Reference Frame modeling nonlinear station motions, *J. Geophys. Res. Solid Earth*, *121*, 6109–6131, doi:10.1002/2016JB013098.

Received 15 APR 2016
Accepted 12 JUL 2016
Accepted article online 18 JUL 2016
Published online 4 AUG 2016

Abstract For the first time in the International Terrestrial Reference Frame (ITRF) history, the ITRF2014 is generated with an enhanced modeling of nonlinear station motions, including seasonal (annual and semiannual) signals of station positions and postseismic deformation for sites that were subject to major earthquakes. Using the full observation history of the four space geodetic techniques (very long baseline interferometry (VLBI), satellite laser ranging (SLR), Global Navigation Satellite Systems (GNSS), and Doppler orbitography and radiopositioning integrated by satellite (DORIS)), the corresponding international services provided reprocessed time series (weekly from SLR and DORIS, daily from GNSS, and 24 h session-wise from VLBI) of station positions and daily Earth Orientation Parameters. ITRF2014 is demonstrated to be superior to past ITRF releases, as it precisely models the actual station trajectories leading to a more robust secular frame and site velocities. The ITRF2014 long-term origin coincides with the Earth system center of mass as sensed by SLR observations collected on the two LAGEOS satellites over the time span between 1993.0 and 2015.0. The estimated accuracy of the ITRF2014 origin, as reflected by the level of agreement with the ITRF2008 (both origins are defined by SLR), is at the level of less than 3 mm at epoch 2010.0 and less than 0.2 mm/yr in time evolution. The ITRF2014 scale is defined by the arithmetic average of the implicit scales of SLR and VLBI solutions as obtained by the stacking of their respective time series. The resulting scale and scale rate differences between the two solutions are 1.37 (±0.10) ppb at epoch 2010.0 and 0.02 (±0.02) ppb/yr. While the postseismic deformation models were estimated using GNSS/GPS data, the resulting parametric models at earthquake colocation sites were applied to the station position time series of the three other techniques, showing a very high level of consistency which enforces more the link between techniques within the ITRF2014 frame. The users should be aware that the postseismic deformation models are part of the ITRF2014 products, unlike the annual and semiannual signals, which were estimated internally with the only purpose of enhancing the velocity field estimation of the secular frame.

1. Introduction

Earth observation is fundamental to addressing scientific challenges pertaining to the quantification of changes that are affecting the Earth system. How is the Earth deforming due to, e.g., plate tectonics, coseismic and postseismic deformations, global geophysical fluid dynamics, or current ice melting? How to accurately determine point positions at the Earth surface that is constantly deforming? What is the rate of sea level rise, its spatiotemporal variability, and its ramification with climate change? Global geodesy is one of the key Earth science disciplines that not only measures changes of the Earth system in space and time but also is the only science that provides the indispensable standard against which the changes and their variability are quantified and properly referenced. In order to answer these scientific questions, fundamental to understanding the Earth dynamics, and also to precisely determine the orbits of the Earth-observing artificial satellites, it is critically important to ensure the continuous availability and updates of an accurate, long-term stable and truly global Terrestrial Reference Frame, such as the International Terrestrial Reference Frame (ITRF). The recent resolution adopted on 26 February 2015 by the General Assembly of the United Nations on the Global Geodetic Reference Frame (GGRF) for Sustainable Development (http://www.un.org/ga/search/view_doc.asp?symbol=A/69/L.53), recognizing the adoption of the ITRF by the scientific community, is a testimony of the critical importance of the reference frame for science and society.

©2016. The Authors.
This is an open access article under the terms of the Creative Commons Attribution-NonCommercial-NoDerivs License, which permits use and distribution in any medium, provided the original work is properly cited, the use is non-commercial and no modifications or adaptations are made.

Table 1. Summary of Submitted Solutions to ITRF[a]

TC	Data Span	Sampling	Solution Type	Constraints	EOPs
IVS	1980.0–2015.0	Daily	Normal equation	None	PM, PMr, LOD, UT1-UTC
ILRS	1983.0–1993.0	Fortnightly	Variance-covariance	Loose	PM, LOD
	1993.0–2015.0	Weekly	Variance-covariance	Loose	PM, LOD
IGS	1994.0–2015.1	Daily	Variance-covariance	Minimum	PM, PMr, LOD
IDS	1993.0–2015.0	Weekly	Variance-covariance	Minimum	PM

[a]PM: polar motion, PMr: polar motion rate, and LOD: length of day.

The space geodetic techniques that contribute to the ITRF construction are Doppler orbitography and radiopositioning integrated by satellite (DORIS), Global Navigation Satellite Systems (GNSS), satellite laser ranging (SLR), and very long baseline interferometry (VLBI). These techniques are organized as scientific services within the International Association of Geodesy (IAG) and known by the International Earth Rotation and Reference Systems Service (IERS) as Technique Centers (TCs): the International DORIS Service (IDS) [*Willis et al.*, 2010], the International GNSS Service, formerly the International GPS Service (IGS) [*Dow et al.*, 2009], the International Laser Ranging Service (ILRS) [*Pearlman et al.*, 2002], and the International VLBI Service (IVS) [*Schuh and Behrend*, 2012]. As none of the four space geodetic techniques is able to provide the full reference frame-defining parameters, the ITRF is demonstrated to be the most accurate reference frame available today, gathering the strengths of the four space geodesy techniques contributing to its construction and compensating for their weaknesses and systematic errors.

The ITRF2014 is an improved release compared to past realizations of the International Terrestrial Reference System (ITRS) [*Altamimi et al.*, 2002a, 2007, 2011], based on reprocessed solutions of the four space geodetic techniques, using data spanning their full observation histories up to the end of 2014. It provides precise quantifications of the coseismic and postseismic displacements and deformations caused by major earthquakes, in particular the devastating recent ones in Chile (2010) and Japan (2011). Its publication coincides not only with the United Nations General Assembly resolution on the GGRF but also with the thirtieth anniversary of the first combined Terrestrial Reference Frame (TRF) using space geodesy data [*Boucher and Altamimi*, 1985]. Since then, the ITRF solutions have improved in accuracy, and each new solution is demonstrated to be superior to past versions, thanks to continuously improved strategy of the ITRF combination and submitted solutions.

The ITRS Center of the IERS, hosted by IGN France, is responsible for the maintenance of the ITRS/ITRF and official ITRF solutions. Two other ITRS combination centers are also generating combined solutions using ITRF input data: Deutsches Geodätisches Forschungsinstitut (DGFI) an der Technischen Universität München (TUM) [*Seitz et al.*, 2012] and Jet Propulsion Laboratory (JPL) [*Wu et al.*, 2015].

2. ITRF2014 Input Data

The ITRF determination fundamentally depends not only on space geodesy solutions but also on the availability of terrestrial measurements, or local surveys, connecting the reference points of geodetic instruments at colocation sites. The following two sections describe the two ensembles of data used in the ITRF2014 construction.

2.1. Space Geodesy Solutions

Table 1 lists the four-technique combined time series submitted to the ITRF2014. It summarizes the data span, the sampling integration for station positions (daily for GNSS, session-wise for VLBI, weekly for DORIS, and fortnightly and weekly for SLR), the solution type (normal equations or variance-covariance), the constraints applied for the reference frame definition (free, loose, or minimum constraints), and the Earth Orientation Parameters (EOPs) provided in addition to station positions. Each per-technique time series is already a combination of the individual analysis center (AC) solutions of that technique. For more details regarding the type of reference frame constraints applied by the techniques, and the minimum constraints concept, in general, the reader may refer to *Dermanis* [2000, 2003], *Sillard and Boucher* [2001], *Altamimi et al.* [2002b, 2004], or to chapter 4 of the IERS Conventions [*Petit and Luzum*, 2010, chap. 4].

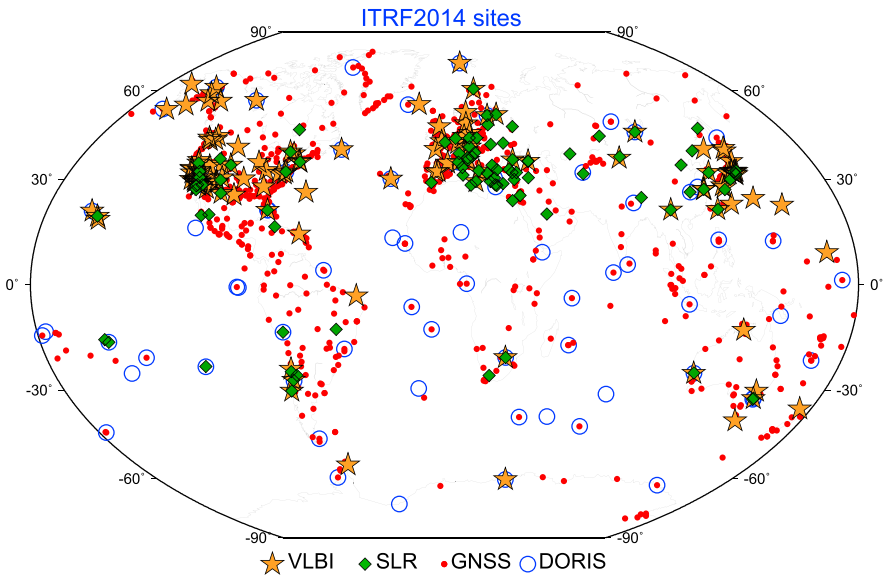

Figure 1. ITRF2014 network highlighting VLBI, SLR, and DORIS sites colocated with GNSS.

The submitted solutions cover the entire observation history of each one of the four techniques. The VLBI contribution involves 5789 session-wise solutions [*Bachmann et al.*, 2015], [*Nothnagel et al.*, 2015]; 407 sessions involving only two stations were discarded from the ITRF2014 processing since they were not designed for the TRF determination. The majority (86%) of the VLBI sessions includes a small number of stations, ranging between 3 and 9. Three hundred ninety-one sessions involve 10–19 stations, eight sessions with 20 stations, while two sessions exceptionally include 21 and 32 stations.

The ILRS solution comprises 244 fortnightly solutions, with polar motion and length of day (LOD) estimated every 3 days for the period 1983.0–1993.0, using LAGEOS I satellite data, and 1147 weekly solutions with daily polar motion and LOD estimates afterward, using data acquired on LAGEOS I and II and ETALON I and II satellites [*Luceri and Pavlis*, 2016].

The IGS-submitted time series comprise 7714 daily solutions, resulting from the second reprocessed campaign, and cover the time period 1994.0–2015.1 [*Rebischung et al.*, 2016]. Two IGS analysis centers have used available and exploitable GLObal NAvigation Satellite System (GLONASS) data in addition to GPS, namely, the Center for Orbit Determination in Europe (CODE) and the European Space Operations Center (ESOC). The starting dates of GLONASS observations are 2002 for CODE and 2009 for ESA when the constellation became almost complete [*Rebischung et al.*, 2016].

The DORIS contribution is a combined time series involving six ACs, using data from all available satellites with an onboard DORIS receiver, and comprises 1140 weekly solutions, spanning the period 1993.0–2015.0 [*Moreaux et al.*, 2016].

Figure 1 illustrates the full ITRF2014 network, comprising 1499 stations located in 975 sites, where about 10% of them are colocated with two, three, or four distinct space geodetic instruments.

2.2. ITRF2014 Local Ties in Colocation Sites

The ITRF combination fundamentally depends on the availability of colocation sites where (1) two or more geodetic instruments of different techniques are operated and (2) local surveys between instrument measuring points are available. Local surveys are usually conducted using terrestrial measurements (direction angles, distances, and spirit leveling) or the GPS technique. Least squares adjustments of local surveys are performed by national agencies operating ITRF colocation sites to provide differential coordinates (local ties) connecting the instrument reference points.

In addition to the local ties used in the ITRF2008 computation, a certain number of local ties used here are new, resulting either from new colocation sites or from new surveys. Thirty-six new surveys were conducted since the release of ITRF2008, and their determined local tie Solution Independent Exchange (SINEX) files,

together with the old ones, were used in the ITRF2014 computation. In total, 139 local tie SINEX files were used in the ITRF2014 versus 104 for ITRF2008. Over the entire ITRF2014 observation history, we used local ties available for 91 colocation sites with two or more technique instruments which were or are currently operating.

The agencies that provided new local tie SINEX files are the following: Geoscience Australia, Istituto Nazionale di Astrofisica, Bologna, Italy, U.S. National Geodetic Survey, Onsala Space Observatory, Sweden, Geodetic Observatory Wettzell/Bundesamts für Kartographie und Geodäsie, Germany, and Geographical Survey Institute (GSI), Japan. All the DORIS colocation sites were readjusted by the IGN survey department in order to generate full SINEX files, including the most recent surveys operated at these sites. All the local tie SINEX files used in the ITRF2014 combination are available at http://itrf.ign.fr/local_surveys.php.

Similar to past ITRF solutions, the local ties used in the ITRF2014 combination are provided in SINEX (Solution Independent Exchange) format with known measurement epochs (with the exception of a few old ties), and 80% of them are available with full variance-covariance information.

Counting the number of colocations between VLBI, SLR, and DORIS, taken by pairs, we find 11 VLBI-SLR, 12 VLBI-DORIS, and 11 SLR-DORIS. These are very small numbers of colocations to allow a reliable combination of these three techniques alone. Therefore, the GNSS network is playing a major role in the ITRF combination, by linking together the three other techniques [*Altamimi and Collilieux*, 2009]. We count in total 212 tie vectors between GNSS and the three other technique reference points: 62 for VLBI, 50 for SLR, and 67 for DORIS. Additional 14 ties were also used between old and current DORIS beacon reference points in DORIS-only sites.

3. ITRF2014 Data Analysis

The procedure adopted for the ITRF formation involves two steps [*Altamimi et al.*, 2002a, 2007, 2011]: (1) stacking the individual time series to estimate a long-term solution per technique comprising station positions at a reference epoch, station velocities, and daily EOPs, and (2) combining the resulting long-term solutions of the four techniques together with the local ties at colocation sites.

3.1. ITRF2014 Time Series Analysis

As detailed in the following sections, the first step of the ITRF2014 analysis, i.e., analyzing and stacking the individual time series, involved for the first time in the context of the ITRF analysis two main innovations dealing with nonlinear station motions: modeling the periodic seasonal signals for stations with sufficient time span and postseismic deformation (PSD) for sites affected by major earthquakes. Modeling the station seasonal signals is accomplished by adding to the combination model the appropriate parameters (coefficients) of sinusoidal functions, while the PSDs were accounted for, before the stacking, by applying parametric models that were first fitted to IGS daily station position time series.

The full equations of the combination model, together with the periodic signals and PSDs, are detailed in the appendices.

The analysis of station position time series used in the first step of the ITRF construction allows capturing not only the linear motions but also all sorts of nonlinear motions: discontinuities, periodic signals, postseismic deformation, velocity changes due to current ice melting, and some other unidentified behaviors of station trajectories. The latter kind of nonlinear motion might be attributed to local effects (e.g., anthropogenic groundwater pumping) or in some cases to systematic errors in the data analysis.

An iterative outlier elimination process was applied in this first step of the stacking of the individual technique solutions, until no observations with normalized residuals larger than 3 remained.

During the stacking of the individual technique time series, nearby stations or multiple segments of the same station in case of discontinuities are constrained to have the same velocity using the following equation:

$$\dot{X}_i = \dot{X}_j \quad (\sigma_v) \tag{1}$$

where i and j are two close-by stations or two consecutive segments of a station with discontinuities. σ_v is the uncertainty constraint at which equation (1) is satisfied, which is chosen to be 10^{-6} m/yr. Such a tight constraint value has the advantage, in the context of time series stacking, to help identify possible velocity

discontinuities for some stations or/and discrepant velocities for nearby stations. In case of such apparent velocity discontinuities, different velocities were estimated before and after the discontinuity events in case of clear apparent slope change. This also holds for some (not all) stations with postseismic deformation behavior.

In order to satisfy the ITRF concept of a linear (secular) frame, it is fundamental to accurately model all kinds of motion and retain the linear trends of the stations, as part of the ITRF parameters.

3.2. Periodic Signals

It is very common to observe periodic signals in the station position time series, which are the manifestation of not only geophysical phenomena, e.g., loading effects caused by the atmosphere, terrestrial water, and ocean circulation [*Dong et al.*, 2002], but also technique systematic errors, such as the draconitic periods for satellite techniques, as shown by *Ray et al.* [2008] for GPS.

It is not expected that the periodic signals present in the station position time series affect the ITRF-defining parameters, especially the origin and the scale [*Collilieux et al.*, 2010], although the velocities of stations with less than 2.5 years of observations might be impacted by these effects [*Blewitt and Lavalée*, 2002]. It is, however, expected that estimating the periodic signals improves the linear station velocity determination, especially for stations with large seasonal signals. Another important advantage of estimating seasonal signals is that it helps the detection of discontinuities in the time series and consequently improves the offset determination.

As described in Appendix B, when stacking time series of station positions, and since our combination model includes a seven-parameter similarity transformation between each input solution and the long-term combined solution, we need to specify how to separate seasonal variations of the transformation parameters from seasonal variations of the station positions. To that end, we chose the internal constraint approach for the translation and scale components, that is, to constrain to zero the periodic signals embedded in the time series of the corresponding transformation parameters. This approach is justified by the fact that it avoids the absorption of part of the station motions by the origin and scale time series. As regard to the rotation parameters, we chose the minimum constraint approach, i.e., imposing no net periodic rotation conditions on a set of well and homogeneously distributed reference stations.

We performed several stacking tests of the individual time series of the four techniques, estimating annual, semiannual signals, as well as a number of draconitic signals, up to the seventh harmonic of the GPS draconitic year (351.4 days). We found that estimating the draconitic signals, in addition to the annual and semiannual signals, has no significant impact on the station linear velocities, compared with the stacking that accounts for annual and semiannual signals only.

Using the IGS daily solutions, we compared the estimated linear site velocities obtained when the annual and semiannual signals are estimated to those obtained when no periodic signals are considered. We found that the horizontal velocity differences are almost all negligible for all stations and are less than 0.05 mm/yr, while the vertical velocity differences are larger and may reach 1 mm/yr as illustrated by Figure 2. The larger vertical velocity differences are for sites with large seasonal signals, with data gaps or with large number of discontinuities. The reduction of the velocity formal errors of about 10% when estimating the seasonal signals could be regarded as an improvement of the velocity determination.

We also performed stacking tests where the station positions of the individual daily or weekly solutions were corrected by a nontidal atmospheric loading (NTAL) model provided by Tonie van Dam (personal communication, 2015), according to the model of the National Center for Environmental Prediction surface pressure. The data are provided on a $2.5 \times 2.5°$ global grid and sampled at 6-hourly rate. A mean of 20 year was removed, and periodic signals less than 26 h were filtered from the station time series to remove the diurnal and semidiurnal atmospheric tides. We interpolated the model to compute the NTAL effect at the central epoch of the daily or weekly observations. Only NTAL of the unmodeled loading effects is evaluated here, because (1) we initially proposed in the ITRF2014 call for participation to apply NTAL model corrections at the stacking step of the ITRF2014 computation and (2) we want to study the performance of the NTAL application versus estimating the annual and semiannual signals. Table 2 lists the averages of the weighted root-mean-square (WRMS) scatters, computed over the time series of daily or weekly station position residuals, for three different stacking tests: standard stacking (STD), stacking with NTAL applied, and stacking where the annual and semiannual frequencies (FREQ2) are estimated with no NTAL model corrections applied. From the WRMS values presented in Table 2, we can see that for all four techniques, the FREQ2 test is

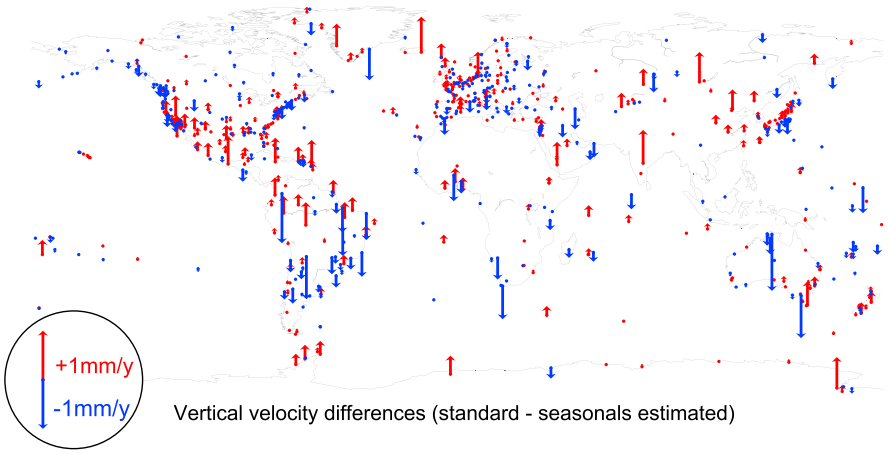

Figure 2. Differences between IGS site velocities obtained from a standard cumulative solution and a solution where annual and semiannual signals are estimated.

performing better than the two other tests, especially in the horizontal components, suggesting that estimating annual and semiannual signals is superior to applying NTAL model. We also computed individual WRMS values for each station resulting from the three stacking tests. In order to compare the performance of the FREQ2 versus NTAL approaches, we plotted in Figure 3 the station WRMS differences for all IGS stations between the NTAL and FREQ2 solutions or (NTAL−FREQ2) values. Positive values as depicted by Figure 3 mean that the WRMS of the FREQ2 solution are smaller than those of the NTAL solution. The percentages of positive values (i.e., better performance for FREQ2 solution) are 84%, 75%, and 59%, in the north, east, and up components, respectively. Similar percentage values are also obtained for the three other techniques. We believe that the better NTAL model performance for 41% of the GNSS/GPS stations in the vertical component is most likely driven by the fact that the NTAL model is able to capture short-period variations which are not accounted for by the annual and semiannual signals. However, although WRMS might not be the only

Table 2. WRMS Averages of Postfit Residuals, in mm, as Result of Three Stacking Tests: Standard Stacking (STD), Stacking With NTAL Applied, and Stacking Where the Annual and Semiannual Frequencies (FREQ2) Are Estimated With No NTAL Model Corrections Applied

Solution	East	North	Up
IVS/VLBI, Session-Wise Sampling			
STD	3.79	3.97	11.00
NTAL	3.75	3.93	10.81
FREQ2	3.74	3.91	10.81
ILRS/SLR, Weekly Sampling			
STD	8.91	10.91	8.18
NTAL	8.90	10.76	8.14
FREQ2	8.83	10.54	8.03
IDS/DORIS, Weekly Sampling			
STD	13.34	10.21	11.84
NTAL	13.32	10.18	11.89
FREQ2	13.17	9.90	11.49
IGS/GNSS, Daily Sampling			
STD	1.90	1.89	5.61
NTAL	1.85	1.84	5.07
FREQ2	1.74	1.71	5.04

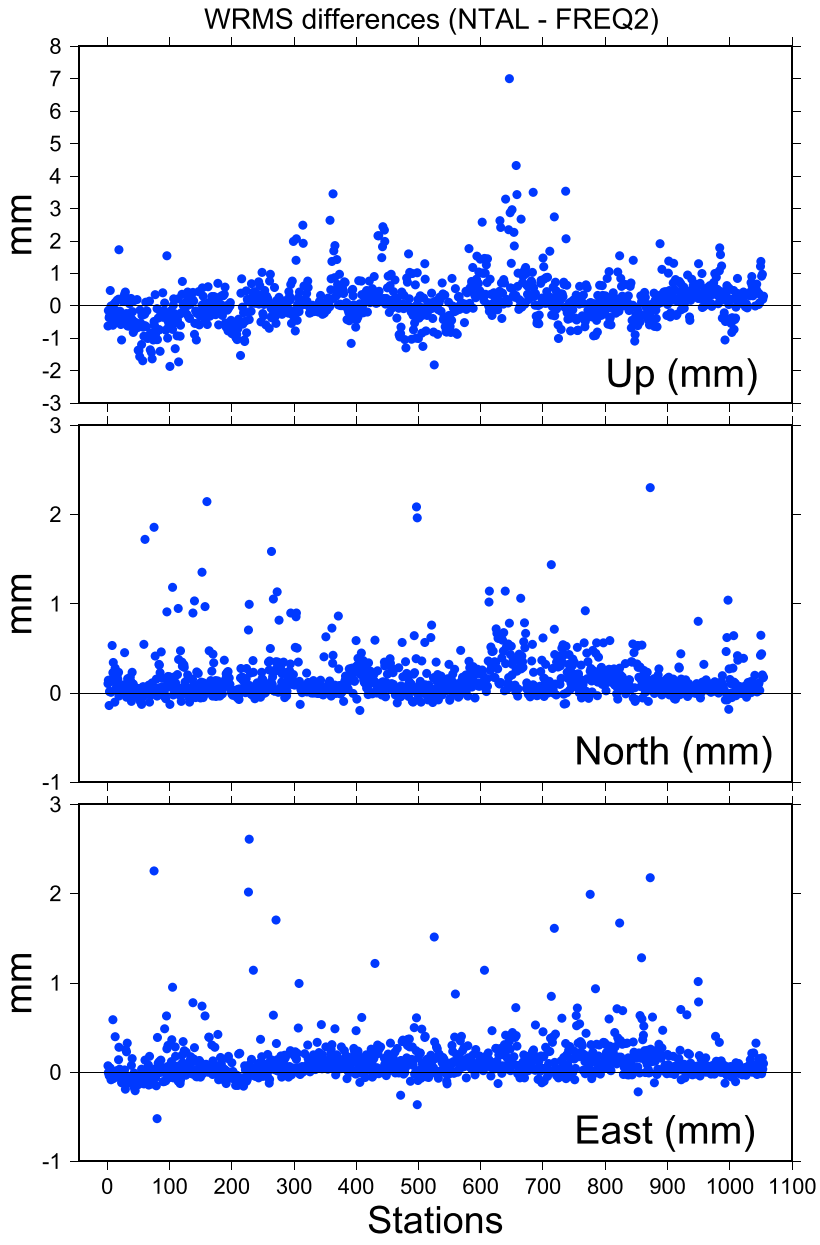

Figure 3. WRMS differences per GNSS station between a solution where nontidal atmospheric loading (NTAL) model was applied before stacking the time series and a solution where annual and semiannual signals were estimated during the stacking without the application of any NTAL corrections.

appropriate discriminator between the two approaches, as could be deduced from Figure 3, the performance of FREQ2 may reach up to 2.5 and 7 mm for some stations in the horizontal and up components, respectively, while the NTAL performance is well below 1 and 2 mm. We also noticed (not shown here) that the remaining station residuals after applying the NTAL corrections still exhibit periodic signals, mainly at the annual and semiannual frequencies, which are most likely reflecting other loading effects, such as ocean circulation and hydrology, or other remaining systematic errors.

For the ITRF2014 solution, based on the results described above, we decided to estimate annual and semiannual signals for stations with sufficient time span (longer than 2 years) for all four techniques and not to apply any external loading model corrections. While more investigations still need to be done, we might consider

for future ITRF solutions to operate both loading model corrections and estimate annual and semiannual signals. However, we note that the approach using periodic functions helps to minimize any bias in the station position estimates, whereas this is not necessarily assured when applying NTAL model.

3.3. Handling of Discontinuities

GNSS station position time series are known to contain discontinuities of various origins, whose correct identification is critical for reliable estimation of the station velocities [*Williams*, 2003]. At present, manual methods for detecting discontinuities in GNSS time series tend to give better results than automated methods [*Gazeaux et al.*, 2013]. In order to identify the discontinuities present in the IGS-submitted time series, we therefore inspected them visually. To each of the time series, we iteratively fitted a model composed of a step function, a constant velocity, annual and semiannual signals, and, when needed, functions describing postseismic deformation behaviors (see the following section), until no discontinuity could be seen in the residual time series. To help in identifying discontinuities and relating them to known events, we made use of two external information sources. On one hand, we collected information about equipment changes from station log files gathered from different sources [*Rebischung et al.*, 2016]. On the other hand, we built a catalog of predicted coseismic offsets following the approach of *Métivier et al.* [2014]. For each earthquake registered in the Global Centroid Moment Tensor Project [*Dziewonski et al.*, 1981; *Ekström et al.*, 2012] during the period 1980–2015, we calculated the coseismic ground deformation at all the ITRF2014 station positions using Okada's algorithm [*Okada*, 1992] and assuming a combination of published earthquake self-similar scaling laws [*Scholz*, 1990; *Mai and Beroza*, 2000; *Yen and Ma*, 2011]. The calculations were made for more than 40,000 earthquakes with magnitude larger than 4, and all computed coseismic displacements larger than 1 mm were flagged as possible causes of discontinuities. In specific cases, a constant velocity was not enough to adequately describe the whole station position time series and velocity discontinuities were introduced in addition to position discontinuities. Most introduced velocity discontinuities describe instantaneous rate changes (mostly due to earthquakes) and are therefore associated with well-determined dates. But about one third (69 out of 187) of the velocity discontinuities were introduced to describe continuous rate changes in the series due to, e.g., slow-slip events or elastic response to current ice melting. In those cases, the dates of the velocity discontinuities were chosen so as to minimize the WRMS of the station residual time series. In the 1054 GNSS station position time series used in the ITRF2014 computation, a total of 1928 position-only or position+velocity discontinuities were identified. Nine hundred forty-two could be related to equipment changes, 567 to earthquakes, 69 were introduced to described continuous rate changes, while the remaining 350 have unknown causes.

For DORIS, SLR and VLBI, we used the same discontinuity epochs as for GNSS at earthquake colocation sites in order to ensure the consistency between the four techniques. The number of discontinuities due to earthquakes are 26 (out of 62), 20 (out of 41), and 40 (out of 49), for DORIS, SLR, and VLBI, respectively. For noncolocation sites, discontinuities were identified by visual inspection of the station position detrended residuals, as results from the individual stacking of the time series where seasonal signals were estimated.

3.4. Postseismic Deformation

After the release of ITRF2008 in 2010, it became more and more obvious that stations impacted by major earthquakes, and in particular the devastating ones in Sumatra (2004), Chile (2010), and Japan (2011), have nonlinear trajectories after these tragic events. Modeling the postseismic deformation (PSD) by piecewise linear functions as in the past ITRF versions is no longer an appropriate approach, at least because the estimated linear velocities of the segmented station time series are imprecise and do not adequately describe the real station postseismic trajectories.

Modeling the PSD for ITRF2014 sites could of course be done using possible available models constructed for each major earthquake individually [*Freed et al.*, 2006; *Pollitz*, 1997, 2014; *Trubienko et al.*, 2013]. However, not all earthquakes impacting the ITRF2014 sites have corresponding published models nor would it be manageable for us to evaluate and test the performance of available models against ITRF2014 input data.

For the ITRF2014 and in order to account for the PSDs of stations subject to major earthquakes, we adopted a more pragmatic approach by fitting parametric models to the ITRF2014 input time series of station positions. The four retained parametric models are (1) (Log)arithmic, (2) (Exp)onential, (3) Log+Exp, and (4) Exp+Exp. It is known that the PSDs have different structures, such as "transient after slip creep" behavior [*Marone et al.*, 1991; *Perfettini and Avouac*, 2004; *Savage et al.*, 2005] tending to follow a logarithmic function or of "viscoelastic relaxation" type [*Savage and Prescott*, 1978; *Pollitz*, 1997] that is better described by an exponential decay.

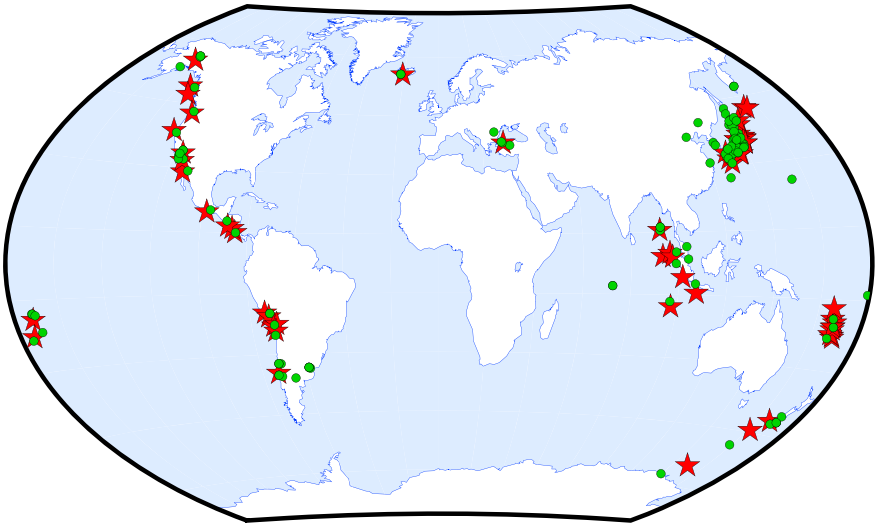

Figure 4. Distribution of earthquake epicenters (red) and ITRF2014 sites (green) impacted by postseismic deformation.

Logarithmic models were used by *Bevis and Brown* [2014] to describe the trajectory of earthquake sites using GPS time series, while *Freed et al.* [2010] used a combination of a logarithmic variation and an exponential decay.

We used the IGS GNSS contributed daily time series to fit parametric models for stations where PSD was judged visually significant, including a few stations impacted by major earthquakes that occurred prior to the start of their observations. The PSD models were fitted separately in each east, north, and up component, simultaneously with piecewise linear functions, annual, and semiannual signals. In case of a series with a unique earthquake causing PSD, 10 different models were first tried: None (0), Log (1), Exp (2), Log+Exp (3), and Exp+Exp (4), each combined with either a position-only or a position+velocity coseismic discontinuity. Among the tested models, those for which the relaxation time of at least one logarithmic or exponential function did not converge were discarded, as well as those leading to at least one insignificant estimated parameter (i.e., smaller than its formal error). Among the remaining models, we finally selected the model with the lowest Bayes Information Criterion [*Schwarz*, 1978], [*Kass and Raftery*, 1995]. For series with $n > 1$ earthquakes causing PSD, all possible 10^n model combinations were similarly tried and the best model combination was selected based on the same criteria.

Figure 4 illustrates in red the location of 59 earthquake epicenters that caused significant PSD at ITRF2014 sites and in green the impacted 123 stations located at 117 sites. We then applied the corrections predicted by the GNSS fitted models to the nearby stations of the three other techniques at earthquake colocation sites, before stacking their respective time series. In order to illustrate the performance of the PSD parametric models, Figure 5 displays the position time series of GNSS/GPS and the colocated VLBI stations at Tsukuba (Japan): in blue the raw data, in green the piecewise linear trajectories given by the ITRF2014 coordinates, and in red the trajectories obtained when adding the parametric PSD model. In that figure, one can see the remarkable fit of the PSD model, not only to the GNSS but also to the VLBI data.

While the ITRF2014 solution provides the usual/classical estimates: station positions at epoch 2010.0, station velocities, and EOPs, the PSD models are also part of the ITRF2014 products. The users should then be aware that they must compute the model corrections, using the equations supplied in Appendix C, to be then added to the ITRF2014 coordinates if the needed position epoch occurs during the postseismic relaxation period. Failing to do so would introduce position errors at the decimeter level for many stations impacted by PSDs. More information and some useful subroutines in Fortran are provided at the ITRF2014 website: http://itrf.ign.fr/ITRF_solutions/2014/.

3.5. ITRF2014 Multitechnique Combination

Once the first step is finalized and long-term frames of the four technique solutions are established, the second step of the ITRF2014 construction is operated. It consists of combining the derived four long-term solutions

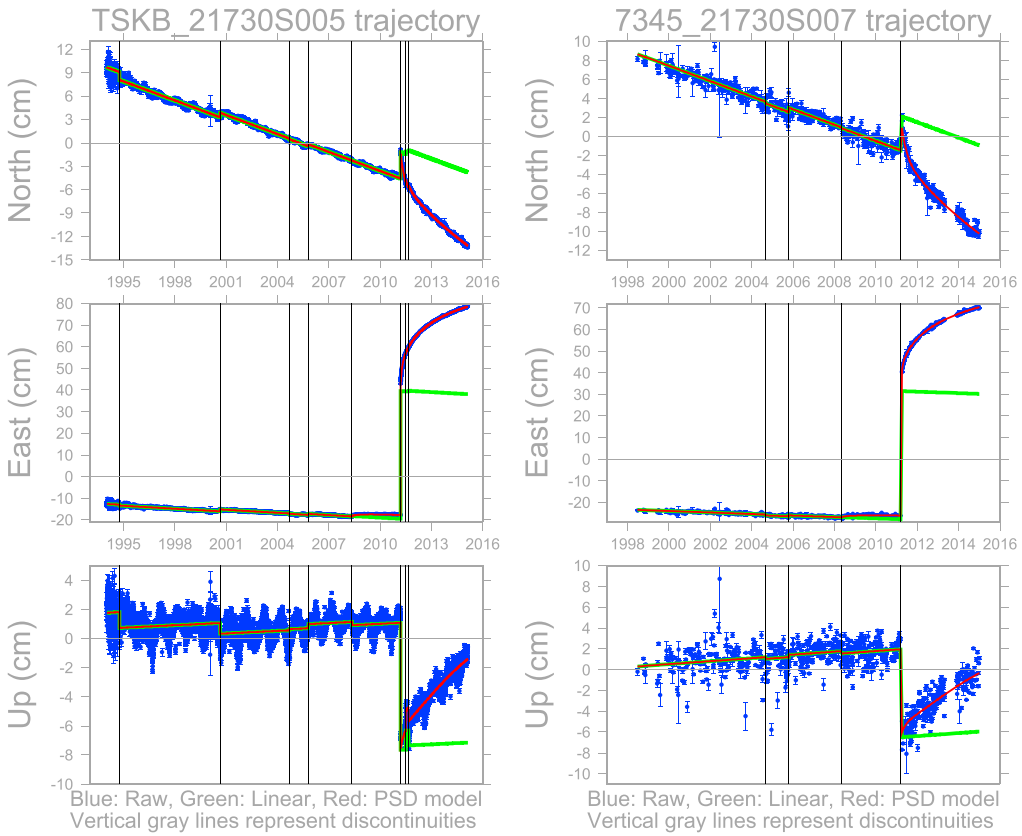

Figure 5. Trajectory of Tsukuba (Japan) site. (left column) GPS and (right column) VLBI. In blue raw data, in green the piecewise linear trajectories given by the ITRF2014 coordinates, and in red the trajectories obtained when adding the parametric PSD model.

together with local ties at colocation sites, involving station positions, velocities, and EOPs. At colocation sites, the seasonal signals of the different technique solutions estimated during the stacking phase were not combined in this second and final step of the ITRF2014 computation. The main reason for this choice is that we noticed large discrepancies for the annual and semiannual terms between techniques and therefore their combination would be difficult to interpret. However, we plan to study these terms separately in future work.

A certain number of test combinations were performed, by varying the weighting of the four technique solutions as well as the local ties. It is worth repeating here what we have discussed in the ITRF2008 paper [*Altamimi et al.*, 2011], which is, it is very difficult to adequately use a mathematically or statistically prescribed method of variance component estimation as the degree of freedom or Helmert method [*Bähr et al.*, 2007]. The main reason is that we have observations and constraints at colocation sites of different types: global space geodesy solutions, local ties (which are local by nature), and velocity equality constraints (cf. equation (1)). In addition, there are significant tie and velocity discrepancies between technique solutions at a number of colocation sites that necessitate an iterative combination and empirical weighting process.

For the ITRF2014, we adopted the following consecutive steps for the relative weighting of the space geodetic technique solutions, the local ties, as well as for the uncertainties of the velocity constraints (σ_v of equation (1)):

1. The long-term solutions of the four techniques were first properly weighted by the a posteriori variance factors obtained from the individual stacking of their respective time series, whose square roots are 2.30, 4.80, 5.02, and 2.62 for GNSS/GPS, VLBI, SLR, and DORIS, respectively.
2. An iterative combination process of the technique velocity fields was performed, as detailed in the following section.

3. Adopting the weighting found in steps 1 and 2, the local tie SINEX files were added with their reevaluated variances, as described in section 3.5.2, and an iterative combination process was performed where discrepant ties were downweighted. During this step, we also ensured that the a posteriori individual variance factors of the four technique solutions should not exceed unity by more than 10%. In order to satisfy this last condition, we found, empirically, that it was necessary to rescale the variance factor of the DORIS long-term solution by a factor of 3.5, while the variance factors of the three other technique solutions were unchanged.
4. The final ITRF2014 adjustment was performed by adding the EOP parameters into the combination. At this final stage, we iterated the combination as necessary and at each iteration rejected any individual input EOP parameter if its normalized residual exceeded a threshold of 3. We also noticed here that when adding the polar motion estimates of the ILRS solution into the combination, it produces a small frame distortion, i.e., increases the position residuals, up to 4 mm with large normalized residuals exceeding the threshold of 3 for a few stations. This behavior needs further investigation in future work and is probably due to a network effect or station positions and polar motion mismatch. In the meantime, in order to avoid that small distortion in the SLR frame, we downweighted the ILRS polar motion estimates by a factor of 2. Doing so stabilized the SLR frame within the overall ITRF2014 combination, and the small distortion disappeared.

3.5.1. Equating Station Velocities at Colocation Sites

An initial combination of the four technique velocity fields was performed (downweighting station positions and local ties) in order to evaluate the level of the velocity agreement between techniques at colocation sites and consequently adopt the appropriate σ_v for the velocity constraint (equation (1)) between colocated reference points. Velocity constraints were added, using equation (1), between a chosen GNSS marker and reference points of the colocated instruments of the three other techniques that are available at these sites. In sites where multiple points of the same technique exist, only one pair of GNSS and other technique points were constrained in velocities, considering that almost all (with a few exceptions) of these multiple points were already constrained to the same velocity during the process of their stacking. The main criterion adopted for the selection of pairs of points (or segments in case of discontinuities) for the velocity constraints was to choose the longest and most stable time series by inspecting their respective detrended residuals. Note that 0.1 mm/yr per component was chosen as an initial value of the σ_v for the velocity constraints, over each component, between GNSS and SLR and VLBI colocated points, while 1 mm/yr was selected for the GNSS and DORIS points. This combination of velocity fields was iterated as necessary, and at each iteration the σ_v of equation (1) was increased for sites where the normalized velocity residual of any of the three components exceeded the threshold of 3. We noticed that selecting smaller initial values for σ_v would lead to an increase in its value for a significant number of colocated sites. Consequently, these initial values represent, for the best sites, the level of the velocity agreement between GNSS and the three other techniques.

3.5.2. Handling of Local Ties

It is worth recalling here that as always performed in previous ITRF combinations, the local ties are used as observations, as described in *Altamimi et al.* [2002b], with a proper weighting for each individual colocation site and local tie SINEX file. In the ITRF2014 combination, we introduced two scaling variance factors for the weighting of local ties: one for the horizontal and one for the vertical component. The justification of this choice is based on the fact that (1) local surveys are often operated using different and independent methods for the horizontal (mainly distance and direction measurements), and the vertical (usually by spirit leveling measurements) components, and (2) the terrestrial vertical measurements are more precise than not only the horizontal but also the vertical estimates of space geodesy.

The initial horizontal and vertical scaling variance factors are computed, for each individual local tie SINEX file, by reevaluating their variances expressed in the local frame, with the condition that the uncertainty per tie vector component (east, north, or up) should not be below 3 mm. The reasons for this condition are that (1) we believe that a local tie between physically inaccessible instrumental measurement reference points is unlikely to be precise to better than 3 mm and (2) the level of agreement between local ties and space geodesy estimates is by far larger than 3 mm for most of the colocation sites.

As for most of the colocation sites, there are discontinuities in the time series of station positions, due not only to earthquakes but also to equipment changes, especially for GNSS. We had to adopt a rationale for selecting the points (or segments) to be tied together. Assigning the tie to the segments spanning the epoch of the survey is not always appropriate, since (1) we have no means to know the real "true" station position among the different discontinuity segments and (2) for many cases we found that the epoch of the survey

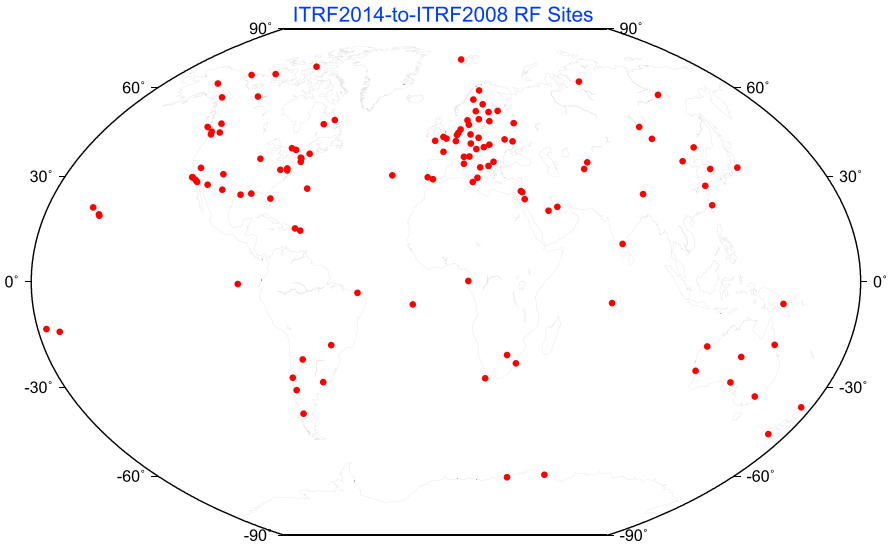

Figure 6. Location of the reference frame sites used in the estimation of the 14 transformation parameters between ITRF2014 and ITRF2008 and their orientation alignment.

coincides with segments with very short time spans. Therefore, we decided to assign the tie to the longest and most stable segments, by inspecting (as for the velocity ties) the detrended time series of the station position residuals. This choice holds for the 36 colocation sites where multiple ties (resulting from surveys conducted at different epochs) are available.

Using all available local ties, we empirically and iteratively downweighted the discrepant ties during the combination process in such a way that the normalized residual does not exceed a threshold of 3 for any of the three components. We choose to downweight the local ties rather than space geodesy solutions in order to avoid contaminating the combined frame-defining parameters by local tie and space geodesy discrepancies and at the same time to preserve the consistency between individual technique solutions and ITRF2014. Counting the percentages of tie discrepancies smaller than 5 mm between terrestrial tie vectors and space geodesy estimates, for stations with reasonable time span (>3 years) of observations, we found 42%, 29%, and 23% for GNSS-VLBI, GNSS-SLR, and GNSS-DORIS, respectively. For completeness, the full list of tie discrepancies is available at the ITRF2014 website.

3.5.3. ITRF2014 Frame Specifications

At this second step, the ITRF2014 is specified by the following frame parameters:

1. *Origin*. The ITRF2014 origin is defined in such a way that there are zero translation parameters at epoch 2010.0 and zero translation rates with respect to the mean origin of the ILRS SLR time series.
2. *Scale*. The scale of the ITRF2014 is defined in such a way that there is zero scale factor at epoch 2010.0 and zero scale rate with respect to the average of the implicit scales and scale rates of VLBI and SLR time series.
3. *Orientation*. The ITRF2014 orientation is defined in such a way that there are zero rotation parameters at epoch 2010.0 and zero rotation rates between ITRF2014 and ITRF2008. These two conditions were applied over a set of 127 reference stations located at 125 sites as illustrated by Figure 6.

4. ITRF2014 Results

4.1. ITRF2014 Origin and Geocenter Motion

As for previous ITRF solutions, the origin of ITRF2014 is defined solely by ILRS SLR data, i.e., satisfying the condition of zero translation and zero translation rate between ITRF2014 and the SLR cumulative solution. The long-term intrinsic origin of the latter is preserved via the usage of internal constraints [*Altamimi et al.*, 2007], over the time span 1993.0–2015.0. Figure 7 illustrates the full time series of the ILRS SLR origin components with respect to ITRF2014. However, when generating the final ILRS SLR cumulative solution used in the ITRF2014 computation, the annual and semiannual signals discernable in Figure 7 were constrained to zero

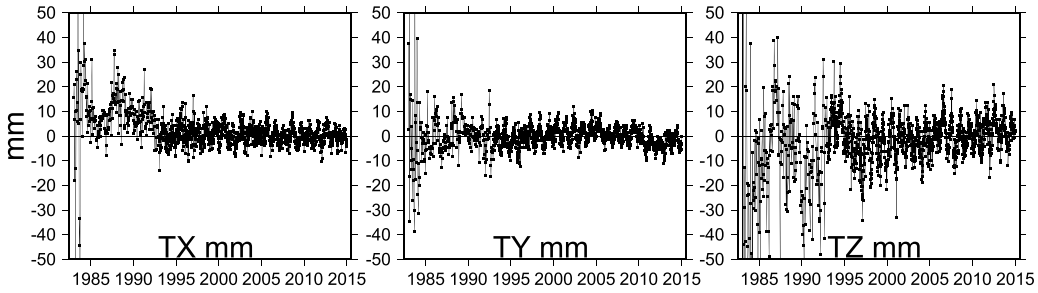

Figure 7. Time series of SLR geocenter components with respect to ITRF2014, in mm.

(over the 1993.0–2015.0 time span) via the usage of internal constraints, as defined by equation (B4). We verified that the small offset in the *Y* component around 2010 that can be seen in Figure 7 biases the long-term ITRF2014 origin along that component by a negligible amount of 0.1 mm/yr.

The performance and accuracy of the ITRF2014 origin could be evaluated by comparison to the ITRF2008 results. The comparison between the two frames showed small translation components at epoch 2010.0, namely, 1.6, 1.9, and 2.4 mm, along the three axes X, Y, Z,, respectively. The translation rates are statistically zero over the three components. These results are an indication of the level of the ITRF origin stability achievable today using SLR data, dominated by LAGEOS I and II observations [*Luceri and Pavlis*, 2016].

Although there exist different definitions of the geocenter motion in the literature, it is defined here as the motion of the Center of Mass (CM) of the total Earth system with respect to the center of figure (CF) of the solid Earth surface, in response to various geophysical fluid displacements within the Earth system, such as the atmosphere, oceans, terrestrial hydrology, and ice sheets [*Wu et al.*, 2012]. While the rate of a possible secular component of the geocenter motion is believed to be less than 1 mm/yr [*Métivier et al.*, 2010, 2011], the amplitude of the annual signal is significant and may reach up to 6 mm along the *Z* axis.

While the ITRF2014 origin follows the average CM, realized by SLR data, only linearly with time, some applications such as satellite precise orbit determination require station coordinates to be referred to the

Table 3. Annual Amplitude (A) and Phase (ϕ) Fitted to the Time Series of the Translation Components and Scale Factors Estimated During the Staking of the Individual Technique Solutions[a]

	T_X		T_Y		T_Z		Scale	
	A	ϕ	A	ϕ	A	ϕ	A	ϕ
TC	(mm)	(deg)	(mm)	(deg)	(mm)	(deg)	(mm)	(deg)
				ITRF2014				
IVS	-	-	-	-	-	-	1.8	245
±							0.1	3
ILRS	2.6	46	2.9	320	5.7	28	0.7	258
±	0.1	3	0.1	2	0.2	2	0.1	8
IDS	2.6	158	3.5	308	0.5	151	0.4	204
±	0.1	3	0.2	2	0.7	71	0.1	13
				ITRF2008 [*Altamimi et al.*, 2011][b]				
IVS	-	-	-	-	-	-	2.2	241
±							0.1	3
ILRS	2.6	42	3.1	315	5.5	22	0.6	255
±	0.1	3	0.1	2	0.3	10	0.1	10
IDS	3.9	147	4.6	340	4.4	295	0.3	206
±	0.2	3	0.3	3	1.1	14	0.1	27

[a] Amplitude and phase are defined by $A\cos(2\pi \cdot t - \phi)$ with t in decimal year.
[b] 180° is added to the phase values of the translation components in order to be consistent with the geocenter motion definition of the IERS Conventions.

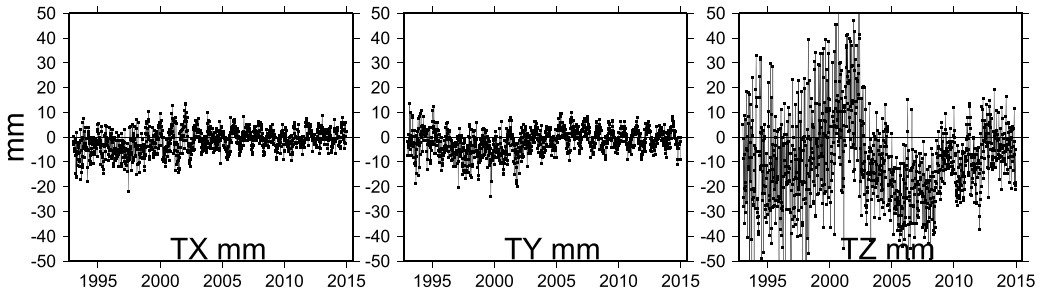

Figure 8. Time series of DORIS geocenter components with respect to ITRF2014, in mm.

instantaneous CM. In order to satisfy these applications, we recommend the usage of an annual geocenter motion model derived from the same SLR data that define the ITRF2014 long-term origin that is to apply to the ITRF2014 station coordinates a correction, δX_{CM}, given by

$$\delta X_{CM} = A\cos(2\pi \cdot t - \phi) \tag{2}$$

so that

$$X_{CM} = X_{ITRF2014} - \delta X_{CM} \tag{3}$$

where the amplitude A and phase ϕ are provided in Table 3 and t is the decimal year. Note that equation (3) is fully consistent with the IERS Conventions [*Petit and Luzum*, 2010, chap. 4]. Moreover, because estimating the scale when stacking the SLR time series may impact the parameters of the annual geocenter motion model [*Collilieux et al.*, 2011], we performed a stacking without estimating the scale parameter. The resulting amplitudes and phases along the three components are similar to, and within the uncertainties of the results listed in Table 3, at the level of 0.3 mm.

For comparison, we reproduce in Table 3 the ITRF2008 results published in *Altamimi et al.* [2011], by adding 180° to the phase values in order to be consistent with the geocenter motion definition of the IERS Conventions. Comparing the annual amplitudes and phases of the SLR translation components with those of ITRF2008, we noticed very similar estimates; i.e., the differences are less than the 3 sigma level for all the values listed in Table 3. The good agreement between ITRF2014 and ITRF2008 modeled geocenter motion, which is at the level of or better than 0.5 mm, is an indication of the intrinsic good performance of the SLR data in sensing the geocenter motion.

The time series of the DORIS geocenter components are plotted in Figure 8 where the annual and semiannual terms are not removed so that SLR (cf. Figure 7) and DORIS results can be compared. It is easy to see from Figures 7 and 8 that there is some similarity for X and Y components between the two techniques, SLR and DORIS, respectively. As listed in Table 3, the geocenter agreement in X and Y components between SLR and DORIS is at the level of 0.6 mm in amplitude, while larger phase discrepancy of 112° is found for the X geocenter component. However, the DORIS Z geocenter is much more scattered than that of SLR and is probably still suffering from some mismodeling issues, such as solar radiation pressure [*Gobinddass et al.*, 2009]. Moreover, from Table 3, we can observe that the amplitude of the DORIS Z geocenter component is discrepant by about 5 mm, compared to SLR estimate, and by about 4 mm compared to ITRF2008 DORIS results.

4.2. ITRF2014 Scale

We followed the same strategy as for ITRF2008 to specify the ITRF2014 scale, that is, to have zero scale and scale rate between ITRF2014 and the arithmetic average of the intrinsic scales of SLR and VLBI solutions. This choice is justified by the fact that we do not have any means to discriminate between the two technique solutions and therefore their simple average is a fair choice that minimizes the scale impact for these two techniques when using the ITRF2014 products. Figure 9 (left) displays the full time series of the scale factors of VLBI, SLR, and DORIS solutions with respect to ITRF2014. However, during the first step of the ITRF2014 computation, i.e., stacking of the individual times series, we made a selection of the weekly SLR and DORIS and daily (session-wise) VLBI solutions to define their respective long-term scales, using the internal constraints approach as described in *Altamimi et al.* [2007]. The justification of this filtering, for the scale definition, is to retain the most precise scale determinations of the three solutions. Therefore, in order to define the respective long-term scales of the three technique cumulative solutions, we excluded the ILRS time series before 1993.0,

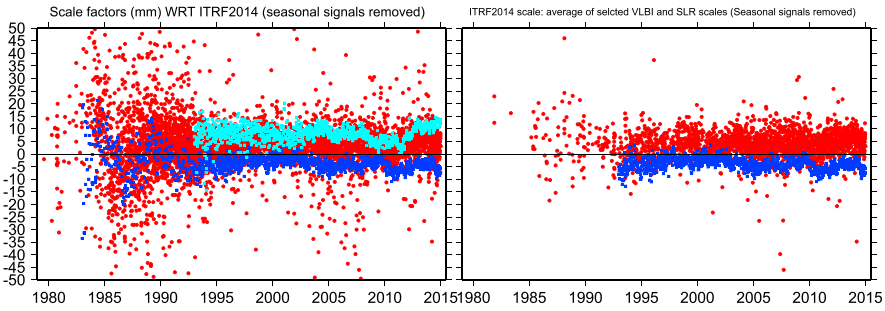

Figure 9. Full time series of (left) scale factors with respect to ITRF2014 and (right) selected SLR and VLBI scale factors whose average defines the ITRF2014 scale, in mm, annual and semiannual signals removed: daily VLBI (red) and weekly SLR and DORIS (blue and light blue), respectively.

the IVS sessions with less than five stations and sessions with regional coverage, and the DORIS data after 2012 because of the offset and drift change after that epoch which can be observed in Figure 9 (left). Figure 9 (right) illustrates the selected VLBI and SLR scale factors whose average defines the ITRF2014 scale. Similar to the *Y* component, the small SLR scale offset around 2010 has negligible impact on the long-term SLR scale of 0.1 mm/yr.

Several combinations of the long-term solutions of the four techniques were tested by varying the local tie weighting and number, such as using those tie vectors with discrepancies with space geodesy solutions smaller than 5 mm. The different combination tests yielded scale factors between SLR and VLBI solutions ranging between 1.4 and 1.7 ppb. We found that the most precise estimation (smallest uncertainty) of the scale factor between the two technique solutions is the one that makes use of all possible and available local tie SINEX files, properly weighted as described in section 3.5.2. The result of the final ITRF2014 combination showed then a scale factor between VLBI and SLR solutions of 1.37 ($\pm$0.10) ppb at epoch 2010.0 and a scale rate of 0.02 ($\pm$0.02) ppb/yr. The ITRF2014 results regarding the level of the scale agreement between SLR and VLBI confirm the ITRF2008 finding and are an indication of the persistent scale offset between the two technique solutions. These results suggest that there is still an urgent need for investigation on the causes of the scale discrepancy, e.g., range biases in case of SLR [*Appleby et al.*, 2016] and possible effects due to VLBI antenna gravity deformations [*Sarti et al.* 2009, 2010].

The scale offset of the DORIS solution with respect to ITRF2014 is 1.16 ppb at epoch 2010.0, and the scale rate is −0.02 ppb/yr. Note that the DORIS scale offset has increased by about 0.5 ppb, compared with ITRF2008 results, which is mainly due to the application of the DORIS ground antenna phase laws by the IDS analysis centers who contributed to the IDS combined solution submitted to the ITRF2014 [*Moreaux et al.*, 2016].

Using the filtered time series of VLBI, SLR, and DORIS scale factors, we computed the annual amplitudes and phases listed in Table 3. Note that the values listed in Table 3 result from the stacking where the periodic signals were not estimated. As can be seen in that table, the ITRF2014 results confirm those of ITRF2008 for the scale amplitudes and phases of the three techniques, at the level of (or better than) 3 sigma. Note, however, that while the VLBI phase is almost similar to SLR one, its amplitude is at least 2 times larger than SLR estimate. This large-amplitude difference can be related, partly, to some mismodeling of the VLBI antenna thermal deformation and partly to the difference of the network shapes of the two techniques. Indeed, the annual scale variation can be interpreted as the mean vertical motion of the implied network of stations [*Collilieux et al.*, 2010], which is different from one technique to another.

4.3. ITRF2014 Earth Orientation Parameters

As for the past ITRF2005 and ITRF2008 solutions, the ITRF2014 rigorous combination provides consistent and fully frame-compatible EOPs: polar motion (PM) components and their daily rates (PM rate), as well as universal time (UT1-UTC) and length of day (LOD). ITRF2014 PM components are the result of the combination of the four technique solutions, PM rate values are determined by combining GNSS and VLBI time series, while UT1-UTC and LOD are determined using VLBI data, uniquely, in order to avoid possible biased estimates from satellite techniques [*Ray*, 1996, 2009].

Figure 10 displays the PM postfit residuals in *x* and *y* components, illustrating the level of agreement between the four techniques, where one can see that GNSS PM series dominate the other technique estimates. The

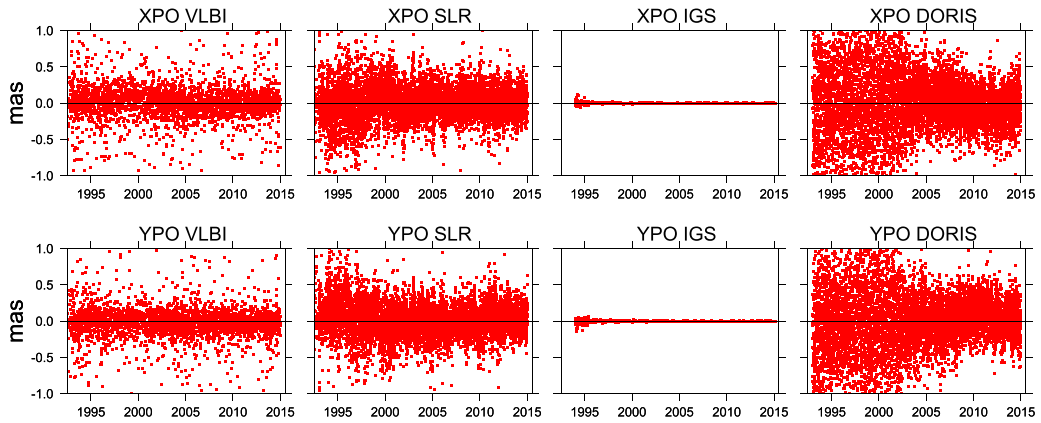

Figure 10. ITRF2014 postfit residuals of polar motion in milliarcseconds.

reader should, however, note that in the ITRF combination, common PM parameters help in tying the four technique solutions, via their relations with the two frame rotation parameters around the *X* and *Y* axes. It should also be noted that estimating station seasonal signals induces a small seasonal signal in the EOP time series. Indeed, using the IGS time series, we compared polar motion estimates resulting from two cumulative solutions, with and without estimating the seasonal signals. The difference between the two polar motion sets is a small sinusoidal curve with amplitude less than 5 μas, far less than the formal errors.

4.4. Transformation Parameters Between ITRF2014 and ITRF2008

In order to ensure the link between ITRF2014 and past ITRF solutions, for many geodetic applications, it is essential to provide to the users the 14 transformation parameters with respect to ITRF2008 and consequently to past ITRF solutions.

The same 127 stations displayed in Figure 6 that were used to ensure the alignment of the ITRF2014 orientation and rate parameters to the ITRF2008 were also used to estimate the transformation parameters between the two frames. The main criterion for the selection of these 127 stations were (1) to have the best possible site distribution; (2) to involve as many as possible VLBI, SLR, GNSS, and DORIS stations; and (3) to have the best agreement between the two frames in terms of postfit residuals of the 14-parameter transformation. Regarding this third criteria, the WRMS values of the 14-parameter similarity transformation fit are 1.8, 1.6, and 2.4 mm in position (at epoch 2010.0) and 0.2, 0.2, 0.3 mm/yr in velocity, in east, north, and vertical components, respectively. Table 4 lists the transformation parameters from ITRF2014 to ITRF2008, to be used with the transformation formula given by equation (4).

$$\begin{cases} \begin{pmatrix} x \\ y \\ z \end{pmatrix}_{i08} = \begin{pmatrix} x \\ y \\ z \end{pmatrix}_{i14} + T + D \begin{pmatrix} x \\ y \\ z \end{pmatrix}_{i14} + R \begin{pmatrix} x \\ y \\ z \end{pmatrix}_{i14} \\ \begin{pmatrix} \dot{x} \\ \dot{y} \\ \dot{z} \end{pmatrix}_{i08} = \begin{pmatrix} \dot{x} \\ \dot{y} \\ \dot{z} \end{pmatrix}_{i14} + \dot{T} + \dot{D} \begin{pmatrix} x \\ y \\ z \end{pmatrix}_{i14} + \dot{R} \begin{pmatrix} x \\ y \\ z \end{pmatrix}_{i14} \end{cases} \tag{4}$$

Table 4. Transformation Parameters at Epoch 2010.0 and Their Rates From ITRF2014 to ITRF2008, to Be Used With Equation (4)

	T_x (mm)	T_y (mm)	T_z (mm)	D (ppb)	R_x (mas)	R_y (mas)	R_z (mas)
	$\dot{T}_x$ (mm/yr)	$\dot{T}_y$ (mm/yr)	$\dot{T}_z$ (mm/yr)	$\dot{D}$ (ppb/yr)	$\dot{R}_x$ (mas/yr)	$\dot{R}_y$ (mas/yr)	$\dot{R}_z$ (mas/yr)
	1.6	1.9	2.4	−0.02	0.00	0.00	0.00
±	0.2	0.1	0.1	0.02	0.06	0.06	0.06
	0.0	0.0	−0.1	0.03	0.00	0.00	0.00
±	0.2	0.1	0.1	0.02	0.06	0.06	0.06

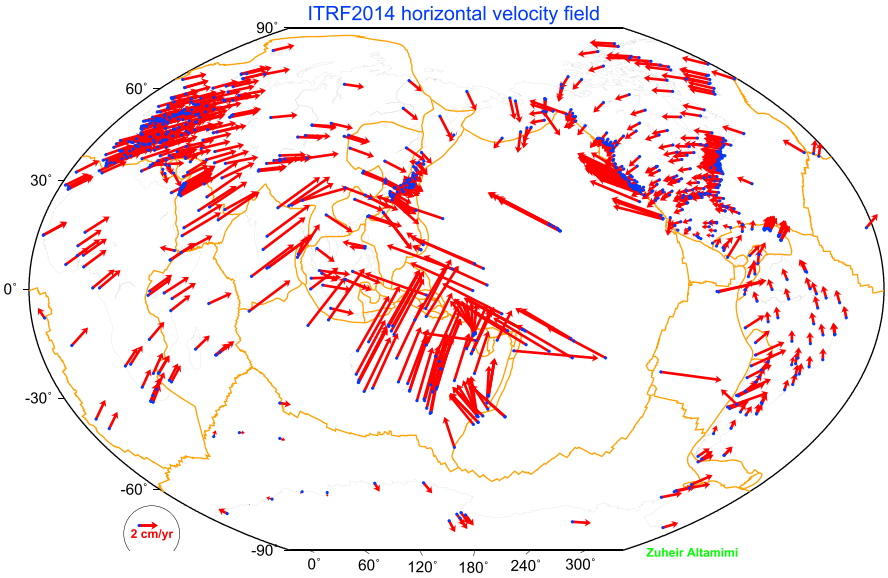

Figure 11. ITRF2014 horizontal site velocities with formal error less than 0.2 mm/yr. Major plate boundaries are shown according to *Bird* [2003].

where *i*08 designates ITRF2008 and *i*14 ITRF2014, T is the translation vector, $T = (T_x, T_y, T_z)^T$, D is the scale factor, and R is the matrix containing the rotation angles, given by

$$R = \begin{pmatrix} 0 & -R_z & R_y \\ R_z & 0 & -R_x \\ -R_y & R_x & 0 \end{pmatrix}$$

The dotted parameters designate their time derivatives. The values of the 14 parameters are those listed in Table 4. Note that the inverse transformation from ITRF2008 to ITRF2014 follows by interchanging (*i*14) with (*i*08) and changing the sign of the transformation parameters.

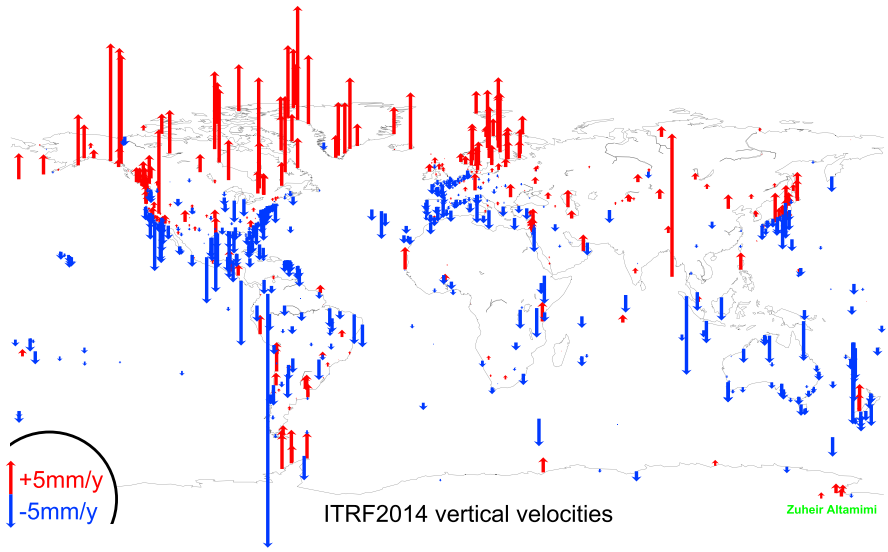

Figure 12. ITRF2014 vertical site velocities with formal error less than 0.2 mm/yr.

4.5. ITRF2014 Velocities

Figures 11 and 12 show the ITRF2014 horizontal and vertical velocity fields for sites with formal error less than 0.2 mm/yr. As the ITRF2014 includes more sites (especially GNSS sites) than ITRF2008, it is anticipated that a more robust plate motion model can be derived, compared to ITRF2008 one [*Altamimi et al.*, 2012], involving more sites on stable parts of the tectonic plates. A dedicated study is underway at the time of writing to develop a plate motion model consistent with ITRF2014.

The ITRF2014 vertical velocities illustrated by Figure 12 show clear regional patterns, especially in North America, Greenland, and Fennoscandia, reflecting the uplift caused by not only Glacial Isostatic Adjustment but also recent or current ice melting. The geophysical interpretation of the ITRF2014 vertical velocities is under investigation, as was the case for ITRF2008 [*Métivier et al.*, 2012] and will be the subject of a dedicated publication.

5. Conclusion

Precisely estimating seasonal signals present in the time series of station positions and modeling postseismic deformation for sites subject to major earthquakes are the main innovations implemented in the ITRF2014 construction.

Although the periodic signals were not expected to influence the ITRF2014 frame-defining parameters (which was numerically verified), estimating the annual and semiannual signals has negligible impact (less than 0.05 mm/yr) on horizontal station velocities, while up to 1 mm/yr vertical velocity changes are observed for some stations that are subject to large seasonal signals or a large number of discontinuities or data gaps in their time series. Estimating the seasonal frequencies performs better (in terms of WRMS reduction) than applying a nontidal atmospheric loading model, for about 80% and 60% of the GNSS stations in the horizontal and vertical components, respectively. Although more investigation still needs to be done, we might consider in future ITRF solutions applying a loading model and at the same time solving for seasonal signals.

Modeling the postseismic deformation for sites impacted by major earthquakes has the potential to accurately describe their actual trajectories and also to adequately infer the linear part of their motions. We showed that the fitted parametric models using IGS GNSS data match the station position time series of the other three techniques at colocation sites, thus enforcing their link and consistency within the ITRF2014 frame.

The ITRF2014 long-term origin is found to be close to that of ITRF2008 at the level of less than 3 mm over the time span of SLR observations (1993.0 onward), reflecting the intrinsic origin accuracy estimated by SLR data. For some applications, e.g., satellite precise orbit determination, where a geocenter motion model is needed to refer ITRF2014 coordinates to the instantaneous Earth Center of Mass (CM), we recommend the usage of the annual geocenter motion model published in this paper that is consistent with the ITRF2008-derived model at the level of 0.5 mm; see Table 3.

The ITRF2014 extensive data analysis, with various test combinations, confirms the persistent scale offset between SLR and VLBI solutions at the level of 1.4 ppb ($\approx$8.7 mm at the equator). The ITRF2014 long-term scale being in the middle of the intrinsic scales of SLR and VLBI minimizes its impact on the results of these two techniques when using ITRF2014 products.

As was already shown with the past ITRF2008 results [*Altamimi et al.*, 2011], there are still significant discrepancies between space geodesy solutions and terrestrial local ties, since more than 50% of the available SLR and VLBI tie vectors to GNSS exhibit residuals larger than 5 mm, and about 30% have residuals larger than 10 mm. We believe that most of these discrepancies are related to technique systematic errors rather than to local ties. While there is still room for improving the technique analysis strategies and results, this should be coupled with improving the ground geodetic infrastructure, toward next generation of SLR and VLBI technologies, with better coverage between the Northern and Southern Hemispheres. VLBI in particular needs to evolve toward more frequent global observational session schedules, with increased number and well-distributed stations.

Maintaining and improving the geodetic infrastructure is the prerequisite for the long-term sustainability of the ITRF, as recognized by the United Nations General Assembly resolution on the global geodetic reference frame for sustainable development.

Appendix A: Combination Model

The main two equations of the combination model implemented in CATREF Software are given below. They involve a 14-parameter similarity transformation, station positions, and velocities, and EOPs and are written as

$$\begin{cases} X_s^i = X_c^i + \left(t_s^i - t_0\right)\dot{X}_c^i \\ \quad + T_k + D_k X_c^i + R_k X_c^i \\ \quad + \left(t_s^i - t_k\right)\left[\dot{T}_k + \dot{D}_k X_c^i + \dot{R}_k X_c^i\right] \\ \dot{X}_s^i = \dot{X}_c^i + \dot{T}_k + \dot{D}_k X_c^i + \dot{R}_k X_c^i \end{cases} \tag{A1}$$

$$\begin{cases} x_s^p = x_c^p + R_{yk} \\ y_s^p = y_c^p + R_{xk} \\ \mathrm{UT}_s = \mathrm{UT}_c - \frac{1}{f} R_{zk} \\ \dot{x}_s^p = \dot{x}_c^p \\ \dot{y}_s^p = \dot{y}_c^p \\ \mathrm{LOD}_s = \mathrm{LOD}_c \end{cases} \tag{A2}$$

where for each point i, X_s^i (at epoch t_s^i) and $\dot{X}_s^i$ are positions and velocities of technique solution s and X_c^i (at epoch t_0) and $\dot{X}_c^i$ are those of the combined solution c. For each individual frame k, as implicitly defined by solution s, D_k is the scale factor, T_k is the translation vector, and R_k is the rotation matrix. The dotted parameters designate their derivatives with respect to time. The translation vector T_k is composed of three origin components, namely, T_x, T_y, T_z, and the rotation matrix of three small rotation parameters, R_x, R_y, and R_z, following the three axes, respectively, X, Y, and Z. t_k is a conventionally selected epoch of the seven transformation parameters. In addition to equation (A1) involving station positions (and velocities), the EOPs are added by equation (A2), making use of pole coordinates x_s^p, y_s^p and universal time UT_s as well as their daily rates $\dot{x}_s^p$, $\dot{y}_s^p$ and LOD_s, where $f = 1.002737909350795$ is the conversion factor from UT into sidereal time. The link between the combined frame and the EOPs is ensured via the three rotation parameters appearing in the first three lines of equation (A2).

Note that equation (A1) uses the linearized form of the general similarity transformation formula, neglecting second- and higher-order terms [*Petit and Luzum*, 2010, chap. 4; *Altamimi and Dermanis*, 2012].

In the first step of the ITRF construction, the first two lines of (A1) and the entire equation (A2) are used to estimate long-term solutions for each technique, by accumulating (rigorously stacking) the individual technique time series of station positions and EOPs. In the second step, the entire two equations are used to combine the long-term solutions obtained in step 1, together with local ties in colocation sites.

Appendix B: Equations for Periodic Signals

The general equation used for the estimation of the periodic signals embedded in the time series of station positions is written as

$$\Delta X_f = \sum_{i=1}^{n_f} a^i \cos(\omega_i t) + b^i \sin(\omega_i t) \tag{B1}$$

where ΔX_f is the total sum of the contributions of all the frequencies considered, n_f is the number of frequencies, $\omega_i = \frac{2\pi}{\tau_i}$, where τ_i is the period of the ith frequency, e.g., annual and semiannual.

Each frequency adds six parameters per station, i.e., $(a_x^i, a_y^i, a_z^i, b_x^i, b_y^i, b_z^i)^T$, in addition to the six position and velocity parameters.

In the case of stacking of time series of station positions, and since the combination model described in Appendix A includes the transformation parameters for each daily or weekly solution with respect to the combined/stacked frame, each frequency introduces seven singularities in the normal equation system, corresponding to the three origin, one scale and three rotation components.

Several mathematical options could be implemented to avoid the seven singularities, such as minimum or internal constraint approaches, in the same way they are usually used for the reference frame definition.

B1. Periodic Signals: Minimum Constraints

In the stacking case, the equations of the minimum constraints approach take the form

$$(A^TA)^{-1}A^T\begin{pmatrix}\delta a_x^i\\ \delta a_y^i\\ \delta a_z^i\end{pmatrix} = (A^TA)^{-1}A^T\begin{pmatrix}a_{xR}^i - a_x^i\\ a_{yR}^i - a_y^i\\ a_{zR}^i - a_z^i\end{pmatrix} \tag{B2}$$

$$(A^TA)^{-1}A^T\begin{pmatrix}\delta b_x^i\\ \delta b_y^i\\ \delta b_z^i\end{pmatrix} = (A^TA)^{-1}A^T\begin{pmatrix}b_{xR}^i - b_x^i\\ b_{yR}^i - b_y^i\\ b_{zR}^i - b_z^i\end{pmatrix} \tag{B3}$$

where A is the well-known design matrix of partial derivatives of the seven transformation parameters and $(a_{xR}^i, a_{yR}^i, a_{zR}^i, b_{xR}^i, b_{yR}^i, b_{zR}^i)^T$ are the reference values for each frequency i that could be taken from an external loading model or as zeros over a set of homogeneously and well-distributed network of stations.

B2. Periodic Signals: Internal Constraints

The inclusion of the transformation parameters in the combination model offers the possibility to use the internal constraint approach as developed in *Altamimi et al.* [2007]. In the stacking case, one possibility is to constrain to zero, internally, the periodic signals embedded in the time series of a given transformation parameter $[P(t_1), \dots P(t_K)]$. In such a case the internal constraint equation takes the form

$$(B^TB)^{-1}B^T[P(t_1), \dots, P(t_K)]^T = 0 \tag{B4}$$

where K is the number of the individual daily or weekly solutions and B is the matrix of partial derivatives given by

$$B = \begin{pmatrix}\cos(\omega_i t_1) & \sin(\omega_i t_1)\\ \vdots & \vdots\\ \cos(\omega_i t_K) & \sin(\omega_i t_K)\end{pmatrix} \tag{B5}$$

Appendix C: Equations of Postseismic Deformation Models

After an earthquake, the position of a station during the postseismic trajectory, X_{PSD}, at an epoch t can be written as

$$X_{\mathrm{PSD}}(t) = X(t_0) + \dot{X}(t - t_0) + \delta X_{\mathrm{PSD}}(t) \tag{C1}$$

where $\dot{X}$ is the station linear velocity vector and $\delta X_{\mathrm{PSD}}(t)$ is the total sum of the postseismic deformation (PSD) corrections at epoch t. For each component $L \in \{E, N, U\}$, we note δL the total sum of PSD corrections expressed in the local frame at epoch t:

$$\delta L(t) = \sum_{i=1}^{n^l} A_i^l \log\left(1 + \frac{t - t_i^l}{\tau_i^l}\right) + \sum_{i=1}^{n^e} A_i^e\left(1 - \mathrm{e}^{-\frac{t-t_i^e}{\tau_i^e}}\right) \tag{C2}$$

where

n^l: number of logarithmic terms of the parametric model;

n^e: number of exponential terms of the parametric model;

A_i^l: amplitude of the ith logarithmic term;

A_i^e: amplitude of the ith exponential term;

τ_i^l: relaxation time of the ith logarithmic term;

τ_i^e: relaxation time of the ith exponential term;

t_i^l: earthquake time (date) corresponding to ith logarithmic term;

t_i^e: earthquake time (date) corresponding to the ith exponential term.

The variance of $\delta L(t)$ is given by

$$\mathrm{var}(\delta L) = C.\mathrm{var}(\theta).C^T \tag{C3}$$

where θ is the vector of parameters of the postseismic deformation model:

$$\theta = \left[A^l_1, \tau^l_1, ..., A^l_{n^l}, \tau^l_{n^l}, A^e_1, \tau^e_1, ..., A^e_{n^e}, \tau^e_{n^e}\right]$$

Note that the values of var(θ) of the parametric models are provided to the users in SINEX format available at the ITRF2014 website.

The elements of the matrix $C = \frac{\partial \delta L}{\partial \theta}$ are computed by the following formulae:

$$\frac{\partial \delta L}{\partial A^l_i} = \log\left(1 + \frac{t - t^l_i}{\tau^l_i}\right) \tag{C4}$$

$$\frac{\partial \delta L}{\partial \tau^l_i} = -\frac{A^l_i\left(t - t^l_i\right)}{\left(\tau^l_i\right)^2\left(1 + \frac{t-t^l_i}{\tau^l_i}\right)} \tag{C5}$$

$$\frac{\partial \delta L}{\partial A^e_i} = 1 - \mathrm{e}^{-\frac{\left(t-t^e_i\right)}{\tau^e_i}} \tag{C6}$$

$$\frac{\partial \delta L}{\partial \tau^e_i} = -\frac{A^e_i\left(t - t^e_i\right)\mathrm{e}^{-\frac{\left(t-t^e_i\right)}{\tau^e_i}}}{\left(\tau^e_i\right)^2} \tag{C7}$$

Note that the PSD models are determined and provided to the users per component $L \in \{E, N, U\}$, independently, and so there are no cross terms (or correlations) between components. However, cross terms between amplitude and relaxation time for each LOG or/and EXP term should be taken into account in the variance calculation of equation (C3). As an example, if for a given station there are three earthquakes that were taken into account in the estimation of the PSD models of its component *E*, and it has one EXP for the first EQ, one EXP for the second EQ, and LOG+EXP for the third EQ, the one line matrix *C* for component *E* in equation (C3) will have eight terms.

Once the variances var(δE), var(δN), var(δU) are computed, the transformation into cartesian is obtained by

$$\mathrm{var}\begin{bmatrix}\delta X\\ \delta Y\\ \delta Z\end{bmatrix} = R.\begin{bmatrix}\mathrm{var}(\delta E) & 0 & 0\\ 0 & \mathrm{var}(\delta N) & 0\\ 0 & 0 & \mathrm{var}(\delta U)\end{bmatrix}.R^T \tag{C8}$$

where *R* is the transformation (Jacobian) matrix from topocentric to geocentric frame and where

$$\begin{bmatrix}\delta X\\ \delta Y\\ \delta Z\end{bmatrix} = R.\begin{bmatrix}\delta E\\ \delta N\\ \delta U\end{bmatrix} \tag{C9}$$

The components E,N,U expressed in the local frame refer to the GRS80 ellipsoid, as recommended by the IERS Conventions [*Petit and Luzum*, 2010, chap. 4].

Acknowledgments
The International Terrestrial Reference Frame (ITRF) is the result of a global collaboration of hundreds of institutions around the world: from the buildup of geodetic observatories, satellite missions, data collection, analysis and combination, to the ITRF generation, thanks to the investment of national mapping agencies, space agencies, universities, and research institutes. The ITRF activities are funded by the Institut National de l'Information Géographique et Forestière (IGN), France, and partly by the Centre National d'études Spatiales (CNES), under TOSCA grant. We are indebted to all Analysis and Combination Centers of the Technique Services of the four techniques which constantly provide data for ITRF solutions which would not exist without their valuable contributions. We thank Tonie van Dam for making available the nontidal atmospheric loading model evaluated in this paper. We acknowledge valuable comments and suggestions provided by the Editor and three anonymous reviewers which improved the content of this article. The input data used in the ITRF2014 computation are available at the NASA Crustal Dynamics Data Information System (CDDIS), http://cddis.nasa.gov/, or through the Technique Centers: http://ids-doris.org/, http://www.igs.org/, http://ilrs.gsfc.nasa.gov/, and http://ivscc.gsfc.nasa.gov/.

References

Altamimi, Z., and X. Collilieux (2009), IGS contribution to the ITRF, *J. Geod.*, *83*(3–4), 375–383, doi:10.1007/s00190-008-0294.
Altamimi, Z., and A. Dermanis (2012), The choice of reference system in ITRF formulation, in *7th Hotine-Marussi Symposium on Mathematical Geodesy, International Association of Geodesy*, vol. 137, pp. 329–334, Springer, Berlin, doi:10.1007/978-3-642-22078-4_49.
Altamimi, Z., P. Sillard, and C. Boucher (2002a), ITRF2000: A new release of the International Terrestrial Reference Frame for Earth science applications, *J. Geophys. Res.*, *107*(B10), 2214, doi:10.1029/2001JB000561.
Altamimi, Z., C. Boucher, and P. Sillard (2002b), New trends for the realization of the International Terrestrial Reference System, *Adv. Space Res.*, *30*(2), 175–184, doi:10.1016/S0273-1177(02)00282-X.
Altamimi, Z., P. Sillard, and C. Boucher (2004), ITRF2000: From theory to implementation, in *V Hotine-Marussi Symposium on Mathematical Geodesy, International Association of Geodesy*, vol. 127, edited by F. Sansò, pp. 157–163, Springer, Berlin, New York, doi:10.1007/978-3-662-10735-5_21.

Altamimi, Z., X. Collilieux, J. Legrand, B. Garayt, and C. Boucher (2007), ITRF2005: A New Release of the International Terrestrial Reference Frame based on time series of station positions and Earth Orientation Parameters, *J. Geophys. Res.*, *112*, B09401, doi:10.1029/2007JB004949.

Altamimi, Z., X. Collilieux, and L. Métivier (2011), ITRF2008: An improved solution of the International Terrestrial Reference Frame, *J. Geod.*, *85*(8), 457–473, doi:10.1007/s00190-011-0444-4.

Altamimi, Z., L. Métivier, and X. Collilieux (2012), ITRF2008 plate motion model, *J. Geophys. Res.*, *117*, B07402, doi:10.1029/2011JB008930.

Appleby, G., J. Rodriguez, and Z. Altamimi (2016), Assessment of the accuracy of global geodetic satellite laser ranging observations and estimated impact on ITRF scale: Estimation of systematic errors in LAGEOS observations 1993–2014, *J. Geod.*, 1–18, doi:10.1007/s00190-016-0929-2.

Bachmann, S., L. Messerschmitt, and D. Thaller (2015), IVS contribution to ITRF2014, in *IAG Commission 1 Symposium 2014: Reference Frames for Applications in Geosciences (REFAG2014)*, pp. 1–6, Springer, Berlin.

Bähr, H., Z. Altamimi, and B. Heck (2007), *Variance Component Estimation for Combination of Terrestrial Reference Frames*, Universität Karlsruhe Schriftenreihe des Studiengangs Geodäsie und Geoinformatik, ISBN: 978-3-86644-206-1.

Bevis, M., and A. Brown (2014), Trajectory models and reference frames for crustal motion geodesy, *J. Geod.*, *88*(3), 283–311, doi:10.1007/s00190-013-0685-5.

Bird, P. (2003), An updated digital model of plate boundaries, *Geochem. Geophys. Geosyst.*, *4*(3), 1027, doi:10.1029/2001GC000252.

Blewitt, G., and D. Lavalée (2002), Effect of annual signals on geodetic velocity, *J. Geophys. Res.*, *107*(B7), 2145, doi:10.1029/2001JB000570.

Boucher, C., and Z. Altamimi (1985), Towards an improved realization of the BIH terrestrial frame, in *Proceedings of the International Conference on Earth Rotation and Reference Frames, MERIT/COTES Rep.*, vol. 2, edited by I. I. Mueller, 551 pp., Ohio State Univ., Columbus, OH.

Collilieux, X., Z. Altamimi, D. Coulot, T. van Dam, and J. Ray (2010), Impact of loading effects on determination of the International Terrestrial Reference Frame, *Adv. Space Res.*, *45*, 144–154, doi:10.1016/j.asr.2009.08.024.

Collilieux, X., T. van Dam, J. Ray, D. Coulot, L. Métivier, and Z. Altamimi (2011), Strategies to mitigate aliasing of loading signals while estimating GPS frame parameters, *J. Geod.*, *86*, 1–14, doi:10.1007/s00190-011-0487-6.

Dermanis, A. (2000), Establishing Global Reference Frames. Nonlinear, Temporal, Geophysical and Stochastic Aspects, in *Gravity, Geoid and Geodynamics*, IAG Symposium, vol. 123, edited by M Sideris, pp. 35–42, Springer, Berlin.

Dermanis, A. (2003), The rank deficiency in estimation theory and the definition of reference systems, in *Hotine-Marussi Symposium on Mathematical Geodesy, IAG Symposia*, vol. 127, edited by F. Sans, pp. 145–156, Springer, Berlin.

Dong, D., P. Fang, Y. Bock, M. K. Cheng, and S. Miyazaki (2002), Anatomy of apparent seasonal variations from GPS-derived site position time series, *J. Geophys. Res.*, *107*(B4), 2075, doi:10.1029/2001JB000573.

Dow, J., R. E. Neilan, and C. Rizos (2009), The International GNSS Service in a changing landscape of Global Navigation Satellite Systems, *J. Geod.*, *83*(3–4), 191–198, doi:10.1007/s00190-008-0300-3.

Dziewonski, A. M., T.-A. Chou, and J. H. Woodhouse (1981), Determination of earthquake source parameters from waveform data for studies of global and regional seismicity, *J. Geophys. Res.*, *86*, 2825–2852, doi:10.1029/JB086iB04p02825.

Ekström, G., M. Nettles, and A. M. Dziewonski (2012), The global CMT project 2004–2010: Centroid-moment tensors for 13,017 earthquakes, *Phys. Earth Planet. Inter.*, *200–201*, 1–9, doi:10.1016/j.pepi.2012.04.002.

Freed, A. M., R. Bürgmann, E. Calais, J. Freymueller, and S. Hreinsdóttir (2006), Implications of deformation following the 2002 Denali, Alaska, earthquake for postseismic relaxation processes and lithospheric rheology, *J. Geophys. Res.*, *111*, B01401, doi:10.1029/2005JB003894.

Freed, A. M., T. Herring, and R. Bürgmann (2010), Steady-state laboratory flow laws alone fail to explain postseismic observations, *Earth and Planet. Sci. Lett.*, *300*(1), 1–10, doi:10.1016/j.epsl.2010.10.005.

Gazeaux, J., et al. (2013), Detecting offsets in GPS time series: First results from the detection of offsets in GPS experiment, *J. Geophys. Res. Solid Earth*, *118*, 2397–2407, doi:10.1002/jgrb.50152.

Gobinddass, M. L., P. Willis, O. de Viron, A. Sibthorpe, J. C. Ries, N. P. Zelensky, Y. Bar-Sever, M. Diament, and R. Ferland (2009), Systematic biases in DORIS-derived geocenter time series related to solar pressure mis-modeling, *J. Geod.*, *83*(9), 849–858, doi:10.1007/s00190-009-0303-8.

Kass, R. E., and A. E. Raftery (1995), Bayes factors, *J. Am. Stat. Assoc.*, *90*(430), 773–795.

Luceri, V., and E. Pavlis (2016), The ILRS contribution to ITRF2014. [Available at http://itrf.ign.fr/ITRF_solutions/2014/doc/ILRS-ITRF2014-description.pdf.]

Mai, M., and G. C. Beroza (2000), Source scaling properties from finite-fault-rupture models, *Bull. Seismol. Soc. Am.*, *90*(3), 604–615.

Marone, C. J., C. H. Scholtz, and R. Bilham (1991), On the mechanics of earthquake afterslip, *J. Geophys. Res.*, *96*(B5), 8441–8452, doi:10.1029/91JB00275.

Métivier, L., M. Greff-Lefftz, and Z. Altamimi (2010), On secular geocenter motion: The impact of climate changes, *Earth Planet. Sci. Lett.*, *3–4*, 360–366, doi:10.1016/j.epsl.2010.05.021.

Métivier, L., M. Greff-Lefftz, and Z. Altamimi (2011), Erratum to "On secular geocenter motion: The impact of climate changes" [Earth Planet. Sci. Lett. 296 (2010) 360–366], *Earth Planet. Sci. Lett.*, *306*(1–2), 136–136, doi:10.1016/j.epsl.2011.03.026.

Métivier, L., X. Collilieux, and Z. Altamimi (2012), ITRF2008 contribution to glacial isostatic adjustment and recent ice melting assessment, *Geophys. Res. Lett.*, *39*, L01309, doi:10.1029/2011GL049942.

Métivier, L., X. Collilieux, D. Lercier, Z. Altamimi, and F. Beauducel (2014), Global coseismic deformations, GNSS time series analysis, and earthquake scaling laws, *J. Geophys. Res. Solid Earth*, *119*, 9095–9109, doi:10.1002/2014JB011280.

Moreaux, G., F. G. Lemoine, H. Capdeville, S. Kuzin, M. Otten, P. Stepanek, P. Willis, and P. Ferrage (2016), Contribution of the International DORIS Service to the 2014 realization of the International Terrestrial Reference Frame, *Adv. Space Res.*, doi:10.1016/j.asr.2015.12.021, in press.

Nothnagel, A., et al. (2015), *The IVS Data Input to ITRF2014. International VLBI Service for Geodesy and Astrometry*, GFZ Data Services, Helmoltz Centre, Potsdam, Germany.

Okada, Y. (1992), Internal deformation due to shear and tensile faults in a half-space, *Bull. Seismol. Soc. Am.*, *82*(2), 1018–1040.

Pearlman, M. R., J. J. Degnan, and J. M. Bosworth (2002), The International Laser Ranging Service, *Adv. Space Res.*, *30*(2), 135–143.

Perfettini, H., and J.-P. Avouac (2004), Postseismic relaxation driven by brittle creep: A possible mechanism to reconcile geodetic measurements and the decay rate of aftershocks, application to the Chi-Chi earthquake, Taiwan, *J. Geophys. Res.*, *109*, B02304, doi:10.1029/2003JB002488.

Petit, G., and B. Luzum (2010), IERS Conventions (2010), *IERS Tech. Note 36*, Verlag des Bundesamts für Kartographie und Geodäsie, 179 pp., Frankfurt am Main, Germany.

Pollitz, F. F. (1997), Gravitational viscoelastic postseismic relaxation on a layered spherical Earth, *J. Geophys. Res.*, *102*(B8), 17,921–17,941, doi:10.1029/97JB01277.

Pollitz, F. F. (2014), Post-earthquake relaxation using a spectral element method: 2.5-D case, *Geophys. J. Int.*, *198*(1), 308–326, doi:10.1093/gji/ggu114.
Ray, J., Z. Altamimi, X. Collilieux, and T. van Dam (2008), Anomalous harmonics in the spectra of GPS position estimates, *GPS Solut.*, *12*(1), 55–64, doi:10.1007/s10291-007-0067-7.
Ray, J. R. (1996), Measurements of length of day using the Global Positioning System, *J. Geophys. Res.*, *101*(B9), 20,141–20,149.
Ray, J. R. (2009), A Quasi-Optimal, Consistent Approach for Combination of UT1 and LOD, in *Geodetic Reference Frames, International Association of Geodesy Symposia*, vol. 134, edited by H. Drewes, pp. 239–243, Springer, Berlin, doi:10.1007/978-3-642-00860-3_37.
Rebischung, P., Z. Altamimi, J. Ray, and B. Garayt (2016), The IGS contribution to ITRF2014, *J. Geod.*, *90*(7), 611–630, doi:10.1007/s00190-016-0897-6.
Sarti, P., C. Abbondanza, and L. Vittuari (2009), Gravity-dependent signal path variation in a large VLBI telescope modelled with a combination of surveying methods, *J. Geod.*, *83*(11), 1115–1126, doi:10.1007/s00190-009-0331-4.
Sarti, P., C. Abbondanza, L. Petrov, and Negusini M. M. (2010), Height bias and scale effect induced by antenna gravity deformations in geodetic VLBI data analysis, *J. Geod.*, *85*(1), 1–8, doi:10.1007/s00190-010-0410-6.
Savage, J. C., and W. H. Prescott (1978), Asthenosphere readjustment and the earthquake cycle, *J. Geophys. Res.*, *83*(B7), 3369–3376.
Savage, J. C., J. L. Svarc, and S.-B. Yu (2005), Postseismic relaxation and transient creep, *J. Geophys. Res.*, *110*, B11402, doi:10.1029/2005JB003687.
Seitz, M., D. Angermann, M. Bloßfeld, H. Drewes, and M. Gerstl (2012), The 2008 DGFI realization of the ITRS: DTRF2008, *J. Geod.*, *86*, 1097–1123.
Schuh H., and D. Behrend (2012), VLBI: A fascinating technique for geodesy and astrometry, *J. Geodyn.*, *61*, 68–80, doi:10.1016/j.jog.2012.07.007.
Schwarz, G. (1978), Estimating the dimension of a model, *Ann. Stat.*, *6*, 461–464.
Sillard, P., and C. Boucher (2001), Review of algebraic constraints in terrestrial reference frame Datum definition, *J. Geod.*, *75*, 63–73.
Scholz, C. H. (1990), *The Mechanics of Earthquakes and Faulting*, Cambridge Univ. Press, Cambridge, U. K.
Trubienko, O., L. Fleitout, J. D. Garaud, and C. Vigny (2013), Interpretation of interseismic deformations and the seismic cycle associated with large subduction earthquakes, *Tectonophysics*, *589*, 126–141, doi:10.1016/j.tecto.2012.12.027.
Williams, S. D. P. (2003), Offsets in Global Positioning System time series, *J. Geophys. Res.*, *108*(B6), 2310, doi:10.1029/2002JB002156.
Willis, P., et al. (2010), The International DORIS Service: Toward maturity, *Adv. Space Res.*, *45*(12), 1408–1420, doi:10.1016/j.asr.2009.11.018.
Wu, X., J. Ray, and T. van Dam (2012), Geocenter motion and its geodetic and geophysical implications, *J. Geodyn.*, *58*, 44–61, doi:10.1016/j.jog.2012.01.007.
Wu, X., C. Abbondanza, Z. Altamimi, T. M. Chin, X. Collilieux, R. S. Gross, M. B. Heflin, Y. Jiang, and J. W. Parker (2015), KALREF—A Kalman filter and time series approach to the International Terrestrial Reference Frame realization, *J. Geophys. Res. Solid Earth*, *120*, 3775–3802, doi:10.1002/2014JB011622.
Yen, Y.-T., and K.-F. Ma (2011), Source-scaling relationship for M 4.6–8.9 earthquakes, specifically for earthquakes in the collision zone of Taiwan, *Bull. Seismol. Soc. Am.*, *101*(2), 464–481, doi:10.1785/0120100046.